

Survival of the quantum depletion of a condensate after release from a harmonic trap in theory and experiment

J. A. Ross,^{1,*} P. Deuar,² D. K. Shin,¹ K. F. Thomas,¹ B. M. Henson,¹ S. S. Hodgman,¹ and A. G. Truscott¹

¹*Laser Physics Centre, Research School of Physics and Engineering,
Australian National University, Canberra, Australia*

²*Institute of Physics, Polish Academy of Sciences, Aleja Lotników 32/46, 02-688 Warsaw, Poland*

Measurements of Tan’s contact in expanding condensate conflict with predictions of the *in situ* quantum depletion. It is unclear how the depletion survives without a condensate, and even appears stronger in the far-field than before the trap release. We confirm experimental observations of a power-law decay in the far-field, consistent with the survival of the quantum depletion. Simulations of our experiment support this conclusion and provide a partial explanation. A gap between the numerical and empirical results is an open question obstructing studies of quantum depletion in the far field.

A profusion of work on quantum degenerate matter is motivated by the promise of the prototypical coherent phenomenon, superfluidity. The underlying mechanism of superfluid formation is the Bose-Einstein condensation of collective excitations, which was realized by Bogoliubov [1]. This finding is of broader importance because the BEC and BCS regimes of superconductivity are characterized by condensation of molecular dimers and of Cooper pairs, respectively.

Bogoliubov formulated the problem of a homogeneous system of interacting bosons in terms of a free Bose gas of collective excitations, constituted by pairs of particles with opposite momenta [2]. The thermal population of quasiparticle modes produces the normal component of a superfluid, while the zero-point population, called the *quantum depletion*, accounts for the large-momentum part of the wavefunction. The Bogoliubov spectrum exhibits a crossover from wavelike phonon modes to single-particle excitations at momenta larger than the speed of sound in the condensate [3], but this description breaks down in strongly interacting systems [4] whereas the Tan relations remain valid in the strongly-correlated regime.

In a modern addition to the theories of quantum matter, Tan explained how s-wave contact interactions modify the short-range pair correlation function and manifests as a power-law decay in the momentum density [5–7]. The contact underpins several universal relations between many-body features and microscopic information in arbitrary spin mixtures at any density, temperature, and geometry [8–12]. Emerging evidence for analogous relations in p-wave scattering [13] and three-body interactions [14] hints at the prospect of new systematic ways to design thermodynamic features by tailoring the interactions between particles.

Two defining properties of Tan’s contact, known as the adiabatic sweep theorem [6] and generalized virial theorem [7], have been decisively verified via radio spectroscopy [15–17] of degenerate Bose [18] and Fermi gases [19, 20]. Bragg spectroscopy has revealed the universal-

ity of scaling relations for the pair correlation function [21] and the behaviour of the contact across the superfluid phase transition [22–24], yielding benchmarks for descriptions of strongly-correlated gases [25].

The Bogoliubov theory has also yielded accurate predictions of the quasiparticle spectrum [2, 4] and of the depleted population in ultracold atomic Bose-Einstein condensates [26, 27] and exciton-polariton condensates in solid substrates [28]. The Bogoliubov spectrum exhibits a crossover from wavelike phonon modes to single-particle excitations at momenta larger than the speed of sound in the condensate [3], but this description breaks down in strongly interacting systems [4]. However, detailed study of the quantum-depleted tails of the momentum distribution has been challenging to date because the tails are beneath the noise floor of optical imaging techniques. A previous experiment sought to use a Feshbach resonance to produce a visible depleted fraction [29], but found that the momentum distribution saturated during expansion and did not display a power-law tail. This was because many-body effects shielded condensed atoms from excitation into the normal component [30, 31].

In contrast, another experiment found unexpectedly large momentum tails in the far-field of a Helium BEC released from a harmonic optical trap [32]. This is particularly surprising because conventional wisdom argues that the density decreases adiabatically during expansion [26], justifying treatment with a hydrodynamic approximation wherein the tails are predicted to vanish [33]. Instead, the study [32] found momentum tails far stronger even than expected in the cloud before release. This contradiction implies that either helium condensates violate the minimal assumptions of Tan’s theory of the contact [5–7], or that far-field momentum measurements are not a straightforward means of examining the quantum depletion even in weakly interacting gases. It is important to verify and overcome this obstacle, as such measurement could play a central role in studying the microscopic physics of superfluids with ultracold gases.

To this end, we revisit the measurement of the momentum distribution of a helium condensate expanding from a harmonic trap. We conducted experiments using

* Corresponding author email: jacob.ross@anu.edu.au

an independent apparatus and analysis, covering a range of densities twice as large as in the prior work [32]. We observe power-law tails in the far field whose amplitude significantly exceeds the predictions of the *in situ* depletion, corroborating the prior work. Our measurements are complemented by simulations of the time-dependence of the momentum distribution using a stochastic Time-Adaptive Bogoliubov (STAB) method in the positive-P framework [34–36]. These show that the non-adiabatic release of the trap is responsible for survival of the depletion, and that the depleted particles acquire additional kinetic energy from the mean-field energy of the condensate during the subsequent adiabatic expansion. These factors result in an amplification of the momentum tails relative to the *in situ* values and are not captured in the hydrodynamic approximation. However, quantitative disagreement between our simulations and experimental data rule out the release energy as a complete explanation for the observed excess counts. We conclude by suggesting an informative complementary approach.

Experiment – Our experimental sequence, depicted schematically in Fig. 1, began with BECs with between 2×10^5 and 5×10^5 ^4He atoms polarized in the $2^3S_1(m_J = 1)$ state and cooled to ~ 300 nK by forced evaporative cooling in a harmonic magnetic trap generated by field coils in a Bi-planar Quadrupole Ioffe configuration [37]. The metastable 2^3S_1 state, denoted He^* , which is 19.8eV above the true ground state [38], enables single-particle detection in the far-field regime and thus affords direct access to microscopic momentum information. The use of a multichannel electron multiplier in combination with a delay-line detector (MCP-DLD) [39] has permitted the observation of many-body momentum correlations [40, 41] and Hanbury Brown-Twiss bunching of both condensed [39, 42–44] and quantum depleted atoms [45].

Investigations of the quantum depletion in He^* are challenging because the absence of a known Feshbach resonance precludes control over the contact $\mathcal{C} \propto (aN_0)^{7/5}\bar{\omega}^{6/5}$ via the scattering length. We therefore test the prediction from Eqn. 1 by varying the density of the gas, $n \propto (N_0\bar{\omega}^3)^{2/5}$. We used two trap configurations with geometric frequencies $\bar{\omega} = 2\pi \cdot 201$ rad Hz $\bar{\omega} = 2\pi \cdot 393$ rad Hz, and varied the endpoint of the RF evaporation ramp to adjust the number of atoms in the condensate. We interleaved the measurements just described with calibrations to determine the shot-to-shot variation in atom number, trapping frequencies, magnetic state transfer efficiency η_0 , and noise contributions (see supplementary materials [36] for more details).

After the trap is switched off, we transferred about one quarter of the atoms to the magnetically insensitive $m_J = 0$ state with a radio-frequency (RF) Landau-Zener sweep to avoid distortion by stray magnetic fields. We deflected the $m_J = \pm 1$ clouds outside the detector field of view by implementing a Stern-Gerlach scheme immediately after the RF pulse. The atoms then ballistically expanded during the ≈ 420 ms freefall to the MCP-DLD

detector ≈ 850 mm below the trap. The atomic velocity components in the in-plane v_x, v_y and vertical v_z directions were reconstructed from the (x, y) position and the time-of-flight of individual atom detection events.

Results – The single-particle detections can be used to construct an estimate of the far-field momentum density. However, estimating parameters of power-law distributions by fitting histograms is prone to bias and underestimation of uncertainties, especially when data is available over less than a decade of dynamic range [46, 47]. The preferred statistical tool for analysing power law distributions are maximum likelihood estimators [46–49], but these are unavailable here because there are multiple sources of detection events, as detailed in [36]. We present an approach that overcomes these issues, yielding the dependence of the tail amplitude on the condensate density in a straightforward way, along with a rigorous uncertainty estimate.

The Tan relations yield an expression for the asymptotic momentum density in terms of the contact \mathcal{C}

$$\lim_{k \rightarrow \infty} \rho(k) = \frac{\mathcal{C}}{k^4} = \frac{64\pi^2 a^2 n_0 N_0}{7 k^4}, \quad (1)$$

where n_0 is the peak density of a condensate of N_0 atoms with s-wave scattering length a [5, 6] (a detailed derivation is given in [36]). Under the hypothesis that the *in situ* depletion survives the expansion, one can integrate

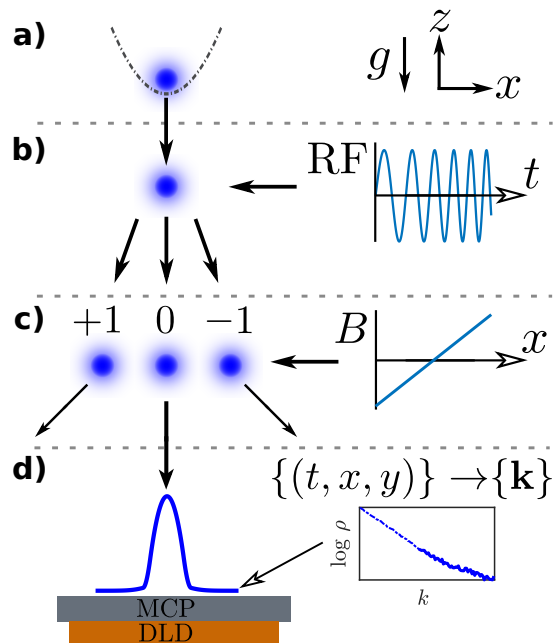


FIG. 1. Sketch of experimental sequence. A BEC is released from a harmonic trap (a) and expands during freefall before being split into a superposition of the $m_J \in \{-1, 0, 1\}$ states (b) by an RF chirp. A magnetic field gradient separates the clouds (c) ensuring that only the magnetically insensitive $m_J = 0$ cloud lands on the detector (d), from which the momentum information is reconstructed. The quantum depletion lies in the dilute tails at large momentum (inset).

Eqn. (1) to predict the expected number of atoms whose wavevector has a modulus in the interval $k \in (k_1, k_2)$,

$$\mathcal{N}_{k_1, k_2} = \int_{k_1}^{k_2} \frac{\rho(k)}{(2\pi)^3} k^2 dk d\theta d\phi \quad (2)$$

$$= \frac{\mathcal{C}}{2\pi^2} \left(\frac{1}{k_1} - \frac{1}{k_2} \right) \quad (3)$$

where the $(2\pi)^3$ Jacobian ensures normalization in k -space. The inverse of Eqn. (3) thus yields an estimation of the tail amplitude (the contact)

$$C_{\text{est}} = \frac{2\pi^2 N_{k_1, k_2}}{\eta} \cdot \frac{k_1 k_2}{k_2 - k_1}, \quad (4)$$

in terms the number of detected atoms N_{k_1, k_2} and the total collection efficiency $\eta \approx 0.3\%$, which accounts for the detector efficiency and geometric factors, as detailed in [36].

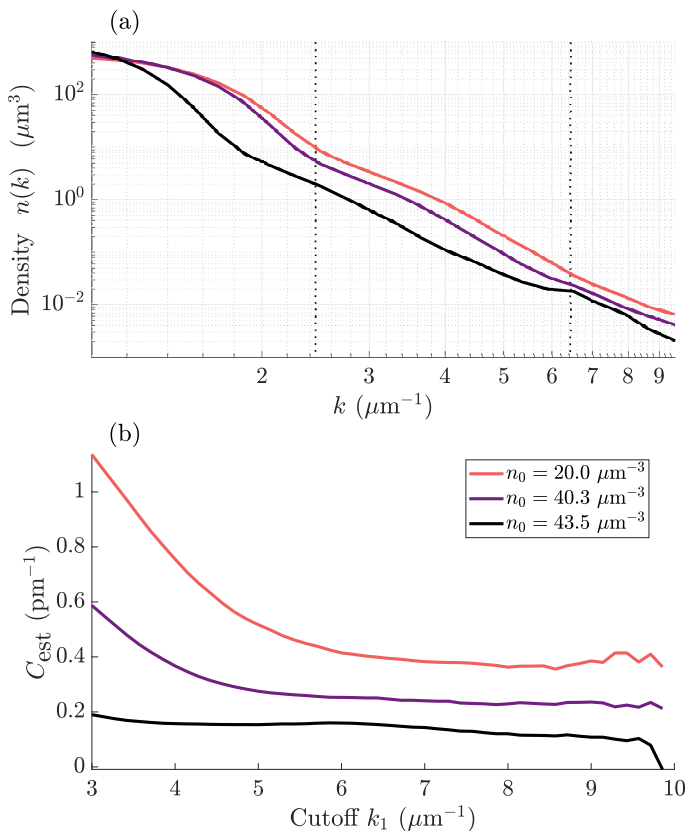


FIG. 2. The empirical density of particle momenta (a) for different peak densities, showing the transition between the condensed, thermal, and depletion regions (indicated for $n_0 = 20 \mu\text{m}^3$ with dotted lines). The number of atoms with wavevector $k \in \{k_1, k_2\}$ within the depletion region yields an estimate of the contact via Eqn. (4). Fixing $k_2 = 10\mu\text{m}^{-1}$, we show C_{est} as a function of the cutoff k_1 (b), which behaves consistently with a k^{-4} -like scaling of the momentum distribution. For each run we choose the k_1 at which C_{est} is the most stable.

Fig. 2 (a) we show the empirical density $n(k)$ for three representative data collection runs. The three regimes of the condensate, thermal part, and depleted particles are visible, spanning over five orders of magnitude in density.

In Fig. 2 (b) we show the estimated contact C_{est} as obtained from Eqn. (4), as a function of the lower bound k_1 with $k_2 = 10 \mu\text{m}^{-1}$. Indeed, Fig. 2 (b) and Eqn. (4) provide a test for the presence of k^{-4} scaling in the momentum density: Because Eqn. 4 is derived assuming a k^{-4} power law, any other behaviour would manifest as a clear dependence of C_{est} on k_1 . The invariance of C_{est} in Fig. 2 therefore confirms the k^{-4} power-law decay in the region of interest.

The value of k_1 must be determined for each run, as the crossover over from thermal to quantum-depleted varies with the condensate density and temperature. We fix k_1 as the point where dC_{est}/dk_1 is minimized, ranging from $4.5 - 6.5\mu\text{m}^{-1}$ between runs. The uncertainty in the C_{est} for each run is the standard error in the mean of C_{est} over all the shots in that run. Across all runs, the average value of C_{est} is 8(1) times *in situ* predictions using Eqn. (3) and calibration parameters. The final uncertainty in this sensitivity is obtained by simple propagation of errors, avoiding the problem of total least-squares regression as encountered in the prior work [32]. The empirical dependence of C_{est} on the atom number and trapping frequencies is shown as a solid line in Fig. 3, with the uncertainty shown as a shaded area. Thus, while the observed momentum distribution is consistent with a k^{-4} asymptotic decay, the amplitude of these tails contradicts the hypothesis of Eqn. (3) by 7σ .

Simulations – To understand the excess contact here and in earlier experiments [32] we performed simulations of the BEC expansion from harmonic traps using the first principles STAB method [34, 35]. The simulations included a cigar-shaped trap (marked CT in Fig. 3) with parameters matched to the experimental conditions (see [36] for details). The in-trap state was consistent with the adiabatic sweep theorem before release from the trap. Following expansion from the cigar trap (CE), the simulated tail amplitude increased and stabilized at a factor of 1.64(9) above the predictions of Eqn. (1). The steady-state occurs within a few hundred microseconds, much sooner than the 2ms delay between the trap release and application of the rf and Stern-Gerlach pulses. To understand the disagreement with earlier theory [33], which predicted no depletion survival, we also investigated the effect of adiabatic expansion on the in-trap depletion by simulating a slow decrease of the transverse trapping frequencies by a factor of two (CS), and found that the in-trap contact decreased roughly as predicted by Eqn. (1) in these instances — see the dashed line in Fig. 4. Details of the method and calculations are in supplementary material [36].

We interpret our results as an indication that the depleted atoms are accelerated by the non-uniform mean-field energy of the condensate during the expansion, and that this contributes to the disagreement between *in situ*

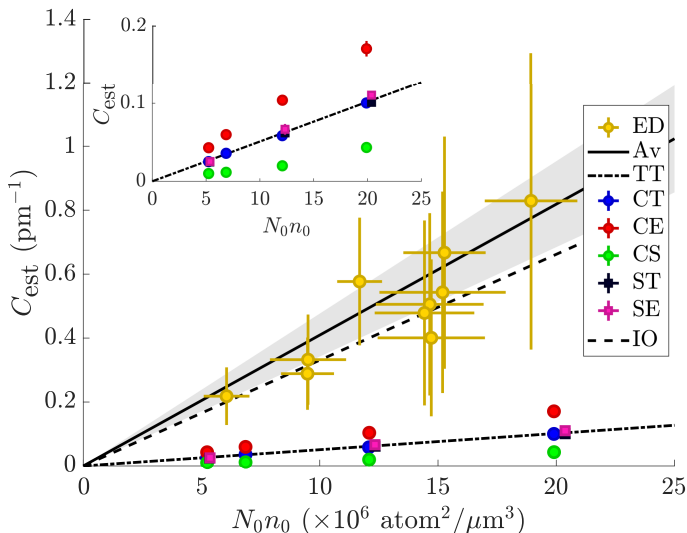


FIG. 3. Comparison of simulations and experiments. The inset is a zoomed view. From our empirical data (ED) we determine the empirical contact C_{est} which is linear in the product $N_0 n_0$ (Eqn. (1)), but 8(1) times more sensitive (Av) than the prediction by the Tan theory (TT). The simulated contact of BECs in a cigar-shaped trap (CT) are consistent with (TT) before release and increases after expansion (CE), but by less than the experiment. A slow relaxation of the tight axes of the cigar trap (CS) leads to a reduction in the simulated contact. Simulations of a spherical trap (ST) show a negligible increase after expansion (SE). The prior He* result [32] (IO) is shown for comparison (dashed line)

and measured contact. In detail, after a quench into the free particle regime, the condensate expands hydrodynamically on timescales of $1/\omega$. This is an adiabatic process for the low momentum depletion, whereby some depleted atoms are absorbed back into the condensate in agreement with [33]. However, the characteristic time for reabsorption is \hbar/gn_0 , slow enough that quasiparticles in the particle branch of the Bogoliubov dispersion have sufficient velocity to escape the expanding cloud without being reabsorbed and thus transition to free atoms.

Moreover, an atom inside the BEC experiences an effective force from the gradient of the mean-field potential $\mathbf{F} = -4\pi\hbar^2 a \nabla n(x)/m$. This endows escaping depleted particles with a greater momentum, increasing the weight of the tails in the far-field. This effect is exacerbated in light atoms like ^4He : because the acceleration scales with $1/m^2$, it would be suppressed by a ~ 500 -fold in ^{87}Rb experiments [29]. This picture is supported by our simulations, in which we observe a decrease in the total number of depleted particles (reabsorption) and a simultaneous increase of the large- k population (forcing). Further, it is much easier for depletion atoms to escape and be accelerated in the transverse x - y directions from an elongated cloud because the distances $R_{TF} = \frac{1}{\omega} \sqrt{2gn_0/m}$ are reduced by $\bar{\omega}/\omega_{x,y}$, whereas the initial mean depletion velocities *in situ* $v \sim \sqrt{2gn_0/m}$ are isotropic: Indeed, spherical clouds (SE) exhibit a much weaker effect

than the elongated clouds (CE) owing to the longer escape time.

Discussion – Our work expands the growing suite of far-field investigations of quantum depletion [32, 45] and confirms that quantum depletion can, remarkably, survive past the lifetime of its original condensate. Our findings clarify that how the depletion can be visible in the far-field momentum distribution here and in earlier experiments, and that the hydrodynamic approximation does not capture sufficient short-wavelength information to make detailed predictions about the high-momentum behaviour. We thus find a partial explanation for the deviation of the far-field distribution from both the predicted *in-situ* depletion and the hydrodynamic reabsorption: The interplay between coherent absorption of Bogoliubov excitations and the dispersal of the chemical potential into kinetic energy, to which helium is particularly sensitive, result in a growth of the k^{-4} tails of the momentum distribution during freefall. However, a mystery remains: Why is the excess depletion some four times greater than accounted for by this picture? This issue should be resolved in order to interpret far-field observations in terms of the *in-trap* physics of interest. This question invites complementary studies of the *in situ* depletion in He* BECs. The important question of whether the far-field anomaly originates in the trapped state or during expansion would be best pursued with Bragg spectroscopy, given the complications of radio spectroscopy of Helium as discussed in [36].

Acknowledgements – The authors thank David

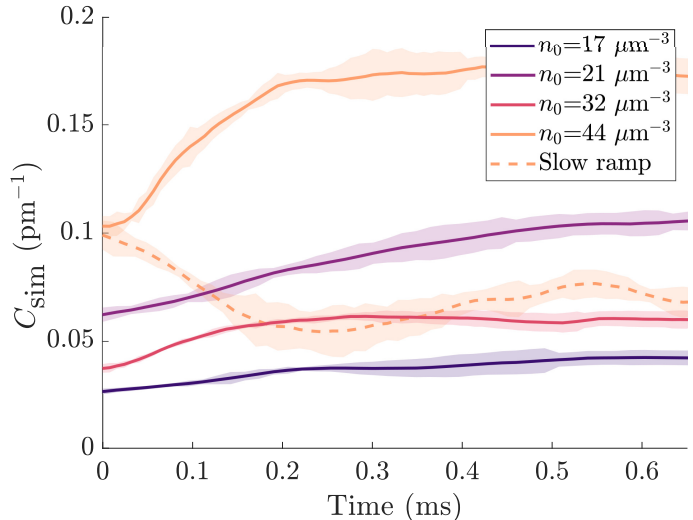


FIG. 4. Simulations of condensates released from a cigar-shaped trap show an increase in contact after the trap release, stabilizing after a time on the order of $1/\omega_x$, several hundred μs . The relative difference between *in-trap* and expanded contact increases with the density of the condensate. For comparison, the experimental control pulses are implemented after 2ms of expansion. In contrast, when the transverse trapping frequencies are reduced by half (dotted line), the *in-situ* contact relaxes.

Clement, Raphael Lopes, Jean Dalibard, and Karen Kherunstyanyan for their helpful discussions. This work was supported by Australian Research Council (ARC) Discovery Project Grants No. DP160102337 and No. DP190103021. S. S. H was supported by DECRA

DE150100315, J.A.R., D. K. S. by the Australian Postgraduate Award (APA), and K.F.T. by the Australian Government Research Training Program (RTP) Scholarship. The simulations by P. D. were supported by National Science Centre (Poland) grants No. 2018/31/B/ST2/01871 and 2012/07/E/ST2/01389.

-
- [1] N. Bogolubov, On the theory of superfluidity, *Journal of Physics USSR* **XI**, 23 (1947).
- [2] J. M. Vogels, K. Xu, C. Raman, J. R. Abo-Shaeer, and W. Ketterle, Experimental observation of the bogoliubov transformation for a bose-einstein condensed gas, *Phys. Rev. Lett.* **88**, 060402 (2002).
- [3] J. Steinhauer, N. Katz, R. Ozeri, N. Davidson, C. Tozzo, and F. Dalfovo, Bragg spectroscopy of the multibranch bogoliubov spectrum of elongated bose-einstein condensates, *Phys. Rev. Lett.* **90**, 060404 (2003).
- [4] R. Lopes, C. Eigen, A. Barker, K. G. Viebahn, M. Robert-de Saint-Vincent, N. Navon, Z. Hadzibabic, and R. P. Smith, Quasiparticle energy in a strongly interacting homogeneous bose-einstein condensate, *Phys. Rev. Lett.* **118**, 210401 (2017).
- [5] S. Tan, Energetics of a strongly correlated fermi gas, *Annals of Physics* **323**, 2952 (2008).
- [6] S. Tan, Large momentum part of a strongly correlated fermi gas, *Annals of Physics* **323**, 2971 (2008).
- [7] S. Tan, Generalized virial theorem and pressure relation for a strongly correlated fermi gas, *Annals of Physics* **323**, 2987 (2008).
- [8] R. Combescot, F. Alzetto, and X. Leyronas, Particle distribution tail and related energy formula, *Phys. Rev. A* **79**, 053640 (2009).
- [9] E. Braaten and L. Platter, Exact relations for a strongly interacting fermi gas from the operator product expansion, *Phys. Rev. Lett.* **100**, 205301 (2008).
- [10] E. Braaten, D. Kang, and L. Platter, Universal Relations for Identical Bosons from Three-Body Physics, *Phys. Rev. Lett.* **106**, 153005 (2011).
- [11] F. Werner and Y. Castin, General relations for quantum gases in two and three dimensions. II. Bosons and mixtures, *Phys. Rev. A* **86**, 053633 (2012).
- [12] F. Werner and Y. Castin, General relations for quantum gases in two and three dimensions: Two-component fermions, *Phys. Rev. A* **86**, 013626 (2012).
- [13] C. Luciuk, S. Trotzky, S. Smale, Z. Yu, S. Zhang, and J. H. Thywissen, Evidence for universal relations describing a gas with p-wave interactions, *Nature Physics* **12**, 599 (2016).
- [14] R. J. Fletcher, R. Lopes, J. Man, N. Navon, R. P. Smith, M. W. Zwierlein, and Z. Hadzibabic, Two- and three-body contacts in the unitary bose gas, *Science* **355**, 377 (2017).
- [15] G. Baym, C. J. Pethick, Z. Yu, and M. W. Zwierlein, Coherence and clock shifts in ultracold fermi gases with resonant interactions, *Phys. Rev. Lett.* **99**, 190407 (2007).
- [16] M. Punk and W. Zwerger, Theory of rf-spectroscopy of strongly interacting fermions, *Phys. Rev. Lett.* **99**, 170404 (2007).
- [17] E. Braaten, D. Kang, and L. Platter, Short-time operator product expansion for rf spectroscopy of a strongly interacting fermi gas, *Phys. Rev. Lett.* **104**, 223004 (2010).
- [18] R. J. Wild, P. Makotyn, J. M. Pino, E. A. Cornell, and D. S. Jin, Measurements of tan's contact in an atomic bose-einstein condensate, *Phys. Rev. Lett.* **108**, 145305 (2012).
- [19] J. T. Stewart, J. P. Gaebler, T. E. Drake, and D. S. Jin, Verification of universal relations in a strongly interacting fermi gas, *Phys. Rev. Lett.* **104**, 235301 (2010).
- [20] Y. Sagi, T. E. Drake, R. Paudel, and D. S. Jin, Measurement of the homogeneous contact of a unitary fermi gas, *Phys. Rev. Lett.* **109**, 220402 (2012).
- [21] E. D. Kuhnle, H. Hu, X.-J. Liu, P. Dyke, M. Mark, P. D. Drummond, P. Hannaford, and C. J. Vale, Universal behavior of pair correlations in a strongly interacting fermi gas, *Phys. Rev. Lett.* **105**, 070402 (2010).
- [22] E. D. Kuhnle, S. Hoinka, P. Dyke, H. Hu, P. Hannaford, and C. J. Vale, Temperature dependence of the universal contact parameter in a unitary fermi gas, *Phys. Rev. Lett.* **106**, 170402 (2011).
- [23] B. Mukherjee, P. B. Patel, Z. Yan, R. J. Fletcher, J. Struck, and M. W. Zwierlein, Spectral response and contact of the unitary fermi gas, *Phys. Rev. Lett.* **122**, 203402 (2019).
- [24] C. Carcy, S. Hoinka, M. Lingham, P. Dyke, C. Kuhn, H. Hu, and C. Vale, Contact and sum rules in a near-uniform fermi gas at unitarity, *Phys. Rev. Lett.* **122**, 203401 (2019).
- [25] A. Rakhimov, Tan's contact as an indicator of completeness and self-consistency of a theory, *Phys. Rev. A* **102**, 063306 (2020).
- [26] K. Xu, Y. Liu, D. E. Miller, J. K. Chin, W. Setiawan, and W. Ketterle, Observation of strong quantum depletion in a gaseous bose-einstein condensate, *Phys. Rev. Lett.* **96**, 180405 (2006).
- [27] R. Lopes, C. Eigen, N. Navon, D. Clément, R. P. Smith, and Z. Hadzibabic, Quantum depletion of a homogeneous bose-einstein condensate, *Phys. Rev. Lett.* **119**, 190404 (2017).
- [28] M. Pieczarka, E. Estrecho, M. Boozarjmehr, O. Bleu, M. Steger, K. West, L. N. Pfeiffer, D. W. Snoke, J. Levinsen, M. M. Parish, A. G. Truscott, and E. A. Ostrovskaya, Observation of quantum depletion in a non-equilibrium exciton-polariton condensate, *Nature Communications* **11**, 429 (2020).
- [29] P. Makotyn, C. E. Klauss, D. L. Goldberger, E. A. Cornell, and D. S. Jin, Universal dynamics of a degenerate unitary bose gas, *Nature Physics* **10**, 116 (2014).
- [30] M. Kira, Hyperbolic bloch equations: Atom-cluster kinetics of an interacting bose gas, *Annals of Physics* **356**, 185 (2015).
- [31] M. Kira, Coherent quantum depletion of an interacting atom condensate, *Nature Communications* **6**, 6624 (2015).

- [32] R. Chang, Q. Bouton, H. Cayla, C. Qu, A. Aspect, C. Westbrook, and D. Clément, Momentum-resolved observation of thermal and quantum depletion in a bose gas, *Phys. Rev. Lett.* **117**, 235303 (2016).
- [33] C. Qu, L. P. Pitaevskii, and S. Stringari, Expansion of harmonically trapped interacting particles and time dependence of the contact, *Phys. Rev. A* **94**, 063635 (2016).
- [34] P. Deuar, J. Chwedeńczuk, M. Trippenbach, and P. Ziń, Bogoliubov dynamics of condensate collisions using the positive-p representation, *Phys. Rev. A* **83**, 063625 (2011).
- [35] K. V. Kheruntsyan, J.-C. Jaskula, P. Deuar, M. Bonneau, G. B. Partridge, J. Ruauadel, R. Lopes, D. Boiron, and C. I. Westbrook, Violation of the cauchy-schwarz inequality with matter waves, *Phys. Rev. Lett.* **108**, 260401 (2012).
- [36] See supplementary materials for details, including Refs. [17, 18, 34, 35, 37, 39, 50–62].
- [37] R. Dall and A. Truscott, Bose–einstein condensation of metastable helium in a bi-planar quadrupole ioffe configuration trap, *Optics Communications* **270**, 255–261 (2007).
- [38] S. S. Hodgman, R. G. Dall, L. J. Byron, K. G. H. Baldwin, S. J. Buckman, and A. G. Truscott, Metastable helium: A new determination of the longest atomic excited-state lifetime, *Phys. Rev. Lett.* **103**, 10.1103/physrevlett.103.053002 (2009).
- [39] A. G. Manning, S. S. Hodgman, R. G. Dall, M. T. Johnson, and A. G. Truscott, The hanbury brown-twiss effect in a pulsed atom laser, *Optics Express* **18**, 18712 (2010).
- [40] S. S. Hodgman, R. G. Dall, A. G. Manning, K. G. H. Baldwin, and A. G. Truscott, Direct measurement of long-range third-order coherence in bose-einstein condensates, *Science*, 1046 (2011).
- [41] R. G. Dall, A. G. Manning, S. S. Hodgman, W. RuG-way, K. Kheruntsyan, and A. G. Truscott, Ideal n -body correlations with massive particles, *Nature physics*, 341 (2013).
- [42] M. Schellekens, R. Hoppeler, A. Perrin, J. Viana Gomes, D. Boiron, A. Aspect, and C. I. Westbrook, Hanbury brown twiss effect for ultracold quantum gases, *Science*, 648 (2005).
- [43] T. Jeltès, J. M. McNamara, W. Vassen, V. Krachmalnicoff, M. Schellekens, A. Perrin, H. Chang, D. Boiron, and C. I. Westbrook, Comparison of the hanbury brown–twiss effect for bosons and fermions, *Nature*, 402 (2007).
- [44] R. G. Dall, S. S. Hodgman, A. G. Manning, M. T. Johnson, K. G. H. Baldwin, and A. G. Truscott, Observation of atomic speckle and hanbury brown–twiss correlations in guided matter waves, *Nature communications* (2011).
- [45] H. Cayla, S. Butera, C. Carcy, A. Tenart, G. Hercé, M. Mancini, A. Aspect, I. Carusotto, and D. Clément, Hanbury brown and twiss bunching of phonons and of the quantum depletion in an interacting bose gas, *Phys. Rev. Lett.* **125**, 165301 (2020).
- [46] A. Clauset, C. R. Shalizi, and M. E. J. Newman, Power-law distributions in empirical data, *SIAM Review* **51**, 661 (2009), arXiv: 0706.1062.
- [47] Y. Virkar and A. Clauset, Power-law distributions in binned empirical data, *The Annals of Applied Statistics* **8**, 89 (2014), arXiv: 1208.3524.
- [48] M. L. Goldstein, S. A. Morris, and G. G. Yen, Problems with fitting to the power-law distribution, *The European Physical Journal B* **41**, 255 (2004).
- [49] R. Hanel, B. Corominas-Murtra, B. Liu, and S. Thurner, Fitting power-laws in empirical data with estimators that work for all exponents, *PLOS ONE* **12**, e0170920 (2017).
- [50] B. M. Henson, X. Yue, S. S. Hodgman, D. K. Shin, L. A. Smirnov, E. A. Ostrovskaya, X. W. Guan, and A. G. Truscott, Bogoliubov-cherenkov radiation in an atom laser, *Phys. Rev. A* **97**, 10.1103/physreva.97.063601 (2018).
- [51] D. K. Shin, B. M. Henson, S. S. Hodgman, T. Wasak, Chwedeńczuk, and A. G. Truscott, Bell correlations between spatially separated pairs of atoms, *Nature communications*, 4447.
- [52] D. K. Shin, J. A. Ross, B. M. Henson, S. S. Hodgman, and A. G. Truscott, Entanglement-base 3d magnetic gradiometry with an ultracold atomic scattering halo, *New Journal of Physics*, 013002 (2020).
- [53] J.-C. Jaskula, M. Bonneau, G. B. Partridge, V. Krachmalnicoff, P. Deuar, K. V. Kheruntsyan, A. Aspect, D. Boiron, and C. I. Westbrook, Sub-poissonian number differences in four-wave mixing of matter waves, *Phys. Rev. Lett.* **105**, 190402 (2010).
- [54] C. J. Dedman, R. G. Dall, L. J. Byron, and A. G. Truscott, Active cancellation of stray magnetic fields in a bose-einstein condensation experiment, *Review of Scientific Instruments* **78**, 024703 (2007).
- [55] S. Moal, M. Portier, J. Kim, J. Dugué, U. D. Rapol, M. Leduc, and C. Cohen-Tannoudji, Accurate determination of the scattering length of metastable helium atoms using dark resonances between atoms and exotic molecules, *Phys. Rev. Lett.* **96**, 10.1103/physrevlett.96.023203 (2006).
- [56] B. M. Henson, D. K. Shin, K. F. Thomas, J. A. Ross, M. R. Hush, S. S. Hodgman, and A. G. Truscott, Approaching the adiabatic timescale with machine learning, *Proceedings of the National Academy of Sciences* **115**, <https://doi.org/10.1073/pnas.1811501115> (2018).
- [57] C. Pethick and H. Smith, *Bose-Einstein condensation in dilute gases*, 2nd ed. (Cambridge University Press, Cambridge, New York, 2008).
- [58] P. J. Leo, V. Venturi, I. B. Whittingham, and J. F. Babb, Ultracold collisions of metastable helium atoms, *Phys. Rev. A* **64**, 042710 (2000).
- [59] W. Vassen, R. P. M. J. W. Notermans, R. J. Rengelink, and R. F. H. J. van der Beek, Ultracold metastable helium: Ramsey fringes and atom interferometry, *Applied Physics B* **122**, 10.1007/s00340-016-6563-0 (2016).
- [60] P. D. Drummond and C. W. Gardiner, Generalised p-representations in quantum optics, *Journal of Physics A: Mathematical and General* **13**, 2353 (1980).
- [61] P. Deuar and P. D. Drummond, Correlations in a bec collision: First-principles quantum dynamics with 150 000 atoms, *Phys. Rev. Lett.* **98**, 120402 (2007).
- [62] A. Sinatra, Y. Castin, and C. Lobo, A monte carlo formulation of the bogolubov theory, *Journal of Modern Optics* **47**, 2629 (2000).
- [63] V. Krachmalnicoff, J.-C. Jaskula, M. Bonneau, V. Leung, G. B. Partridge, D. Boiron, C. I. Westbrook, P. Deuar, P. Ziń, M. Trippenbach, and K. V. Kheruntsyan, Spontaneous four-wave mixing of de broglie waves: Beyond optics, *Phys. Rev. Lett.* **104**, 150402 (2010).
- [64] R. J. Lewis-Swan and K. V. Kheruntsyan, Proposal for demonstrating the hong–ou–mandel effect with matter waves, *Nature Commun.* **5**, 3752 (2014).
- [65] R. J. Lewis-Swan and K. V. Kheruntsyan, Proposal for a motional-state bell inequality test with ultracold atoms,

- Phys. Rev. A **91**, 052114 (2015).
- [66] P. Deuar, T. Wasak, P. Ziń, J. Chwedeńczuk, and M. Trippenbach, Tradeoffs for number squeezing in collisions of bose-einstein condensates, Phys. Rev. A **88**, 013617 (2013).
 - [67] P. Deuar, J.-C. Jaskula, M. Bonneau, V. Krachmalnicoff, D. Boiron, C. I. Westbrook, and K. V. Kheruntsyan, Anisotropy in s-wave Bose-Einstein condensate collisions and its relationship to superradiance, Phys. Rev. A **90**, 033613 (2014).
 - [68] P. Deuar, J. D. Ross, and A. G. Truscott (2021), in preparation.
 - [69] P. Deuar, Multi-time correlations in the positive-P, Q, and doubled phase-space representations (2020), arXiv:2011.10107 [quant-ph].
 - [70] J. Ruostekoski and A. D. Martin, The truncated wigner method for bose gases, in *Quantum Gases* (Imperial College Press, 2013) Chap. 13, pp. 203–214.
 - [71] A. Sinatra, Y. Castin, I. Carusotto, C. Lobo, and E. Witkowska, Number-conserving stochastic approaches for equilibrium and time-dependent bose gases, in *Quantum Gases* (Imperial College Press, 2013) Chap. 14, pp. 215–228.
 - [72] A. D. Martin and J. Ruostekoski, Nonequilibrium quantum dynamics of atomic dark solitons, New Journal of Physics **12**, 055018 (2010).
 - [73] A. D. Martin and J. Ruostekoski, Quantum and thermal effects of dark solitons in a one-dimensional bose gas, Phys. Rev. Lett. **104**, 194102 (2010).
 - [74] A. Sinatra, C. Lobo, and Y. Castin, The truncated wigner method for bose-condensed gases: limits of validity and applications, Journal of Physics B: Atomic, Molecular and Optical Physics **35**, 3599 (2002).
 - [75] A. A. Norrie, R. J. Ballagh, and C. W. Gardiner, Quantum turbulence and correlations in bose-einstein condensate collisions, Phys. Rev. A **73**, 043617 (2006).
 - [76] P. Deuar, *First-principles quantum simulations of many-mode open interacting Bose gases using stochastic gauge methods*, Ph.D. thesis, University of Queensland, arXiv:cond-mat/0507023 (2005).
 - [77] P. D. Drummond and B. Opanchuk, Initial states for quantum field simulations in phase space, Phys. Rev. Research **2**, 033304 (2020).
 - [78] J. Pietraszewicz, M. Stobińska, and P. Deuar, Correlation evolution in dilute bose-einstein condensates after quantum quenches, Phys. Rev. A **99**, 023620 (2019).
 - [79] L. P. Pitaevskii and S. Stringari, *Bose-Einstein condensation and superfluidity*, first edition ed., International series of monographs on physics No. 164 (Oxford University Press, Oxford, United Kingdom, 2016) oCLC: ocn919186901.
 - [80] J. Decamp, M. Albert, and P. Vignolo, Tan’s contact in a cigar-shaped dilute bose gas, Phys. Rev. A **97**, 033611 (2018).

Survival of the quantum depletion of a condensate after release from a harmonic trap in theory and experiment

Supplementary materials

J. A. Ross, P. Deuar, D. K. Shin, K. F. Thomas, B. M. Henson, S. S. Hodgman, A. G. Truscott

I. DETECTION

We use a Roentdek DLD80 multichannel plate and delay-line detector stack [39] with a quantum efficiency of $\approx 8\%$, and space and time resolutions of $100 \mu\text{m}$ and $3 \mu\text{s}$, respectively [50]. After the atoms are released from the trap, they fall 859mm to the detector stack, which registers the arrival times and positions (t_i, x_i, y_i) of each atom, indexed by i . The centre of mass of the cloud arrives after a $\tau = 417\text{ms}$ time of flight following the trap switch-off. The velocity of each atom relative to the centre of mass of the cloud is given by $(v_x, v_y, v_z) = t_i^{-1}(x_i - \bar{x}, y_i - \bar{y}, g_0(\tau^2 - t_i^2))$, where g_0 is the local gravitational acceleration and the overbar denotes the within-shot average. The velocity conversion assumes a point source but carries a negligible error of a few ppm as the in-trap BEC size is smaller than the detector resolution. We centre the counts from each realization and detection sequence (termed a *shot*) and transform the counts from cartesian velocity space to spherical polar coordinates with radius k (in m^{-1}), polar angle θ and elevation angle ϕ , relative to the centre of the cloud, where the velocity-to-wavevector transformation follows from $\mathbf{p} = m\mathbf{v} = \hbar\mathbf{k}$.

The detector efficiency was $\chi = 0.08(2)$, as we determined from the collection efficiency of correlated atoms on the opposite sides of scattering halos [51–53]. The solid angle in k-space available to detect the depleted tails is limited by the 40mm radius of the circular detection surface. The field of view of our detector in the (x, y) plane is $\lesssim 5 \times 10^6 \text{ m}^{-1}$, which is only just sufficient to reach past the edge of the thermal region. Therefore, we sample data from the segments of the sphere with elevation angle $|\phi| > \pi/3$ rad and $|k| < 10^7 \text{ m}^{-1}$, centred on the BEC, which encompasses a total solid angle of $0.13 \times 4\pi$ steradians. The noise floor is set by the detector's dark count rate of $0.56(1) \text{ Hz cm}^{-2}$, which contributes an average of $0.4(2)$ counts to the region of interest (ROI) per shot. A summary of the results for each data run are shown in Tab. I.

II. TRAP CONFIGURATION AND CALIBRATION

We prepared our BECs with via forced evaporative cooling in a harmonic magnetic trap with trap frequencies (425, 425, 45) Hz and a DC bias stabilized by our auxiliary field compensation coils [37, 54]. For the tight

trap we increased the coil current after the cooling sequence to obtain trapping frequencies (902, 895, 71) Hz, ramping the field as a sigmoid step function to minimize in-trap oscillations. The trap remained on for 150ms before switching the trap off with a $1/e$ time of $\approx 38\mu\text{s}$. The condensates were allowed to expand for 2ms before we transferred some of the condensate into the magnetically insensitive $m_J = 0$ state via Landau-Zener sweep to prevent distortion by stray magnetic fields. The RF pulse was created by a function generator, amplified, and applied to the experiment chamber by a coiled antenna inserted into the BiQUIC coil housing. The pulse swept from 1.6-2.6MHz over 1ms and was centred on the fine structure resonance between the m_J states. The transfer efficiencies η_j for each of the $m_J = j$ states is discussed in the next section. The sweep was 10^6 -fold wider than the Doppler broadening of the BEC which ensured uniform transfer at all momenta. Immediately after the RF sweep, the bias coils are switched off and auxiliary push coils in the vertical (Z) and weak horizontal (X) axes are activated using a fast MOSFET switch to implement a Stern-Gerlach separation of the $m_J = -1, 0,$ and $+1$ pulses.

A. Determining transfer efficiency

To calibrate the transfer efficiencies, we applied a weaker Stern-Gerlach than for the depletion measurement, resolving each m_J cloud on the detector, as illustrated in Fig. 5.

The efficiencies η_J cannot be calculated by counting the atoms in each cloud because the detector saturates during the peak condensate flux, but we can compare the thermal parts. We align each cloud along the time (Z) axis and compute the pointwise fraction of the atomic flux $\phi(t)$ accounted for by each cloud, $\eta_j(t) = \phi_j(t) / \sum_j \phi_j(t)$, as depicted in Fig. 5. The ratio of densities between the clouds is roughly constant in the thermal part, indicating the absence of important saturation effects and a spin transfer that is independent of k . The fraction of the original cloud transferred into each m_J state is determined by taking the average $\langle \eta_j(t) \rangle$ over the thermal tails. We find these efficiencies are approximately 74%, 24%, and 2% in all runs for the $m_J = +1, 0,$ and -1 states, respectively.

While the $m_J = 0$ and $m_J = 1$ clouds clearly saturate the detector, the small fraction ($\approx 2\%$) of the atoms transferred to the $m_J = -1$ state does not (Fig. 5 (d)). A bimodal fit to the condensed and thermal parts, plus constant background, yields an estimate of the thermal and condensed fractions.

B. Analysis of spin transfer measurements

In early tests of our measurement sequence we noticed a contamination of the signal by spurious counts. We

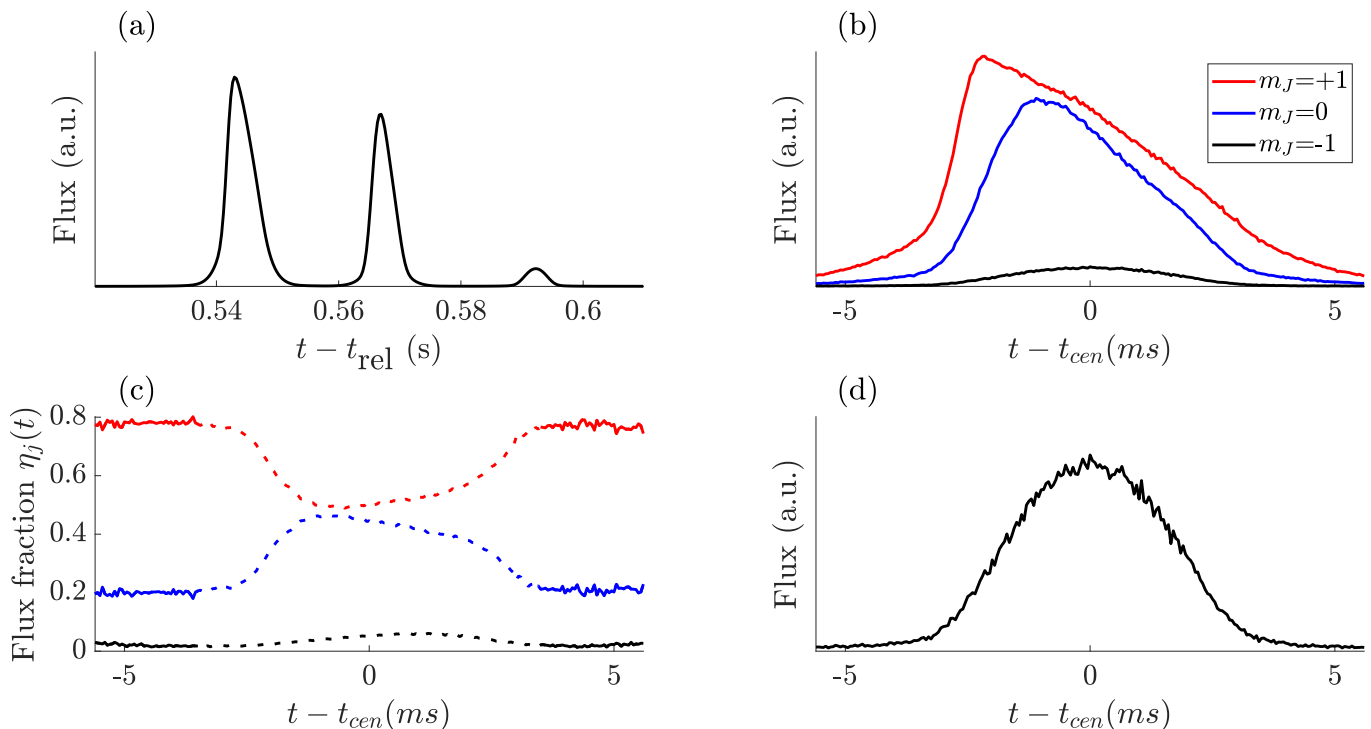


FIG. 5. Determining the RF transfer efficiency. The time-of-flight profiles of each pulse are resolved (a) by applying a weak Stern-Gerlach pulse during the time of flight. The pulses are aligned with respect their centre-of-mass (b) and used to determine the pointwise fraction ((c), dotted line). Detector saturation is evident in the peaks (dashed lines), but not in the thermal tails (solid lines), which are used to compute the transfer efficiency. Because of its lower flux, the $m_J = -1$ pulse does not show evidence of saturation (d) and is used to determine the thermal fraction.

inferred these were remnant counts from the $m_J = +1$ cloud as they were still visible when we ran an experimental sequence without the Landau-Zener transfer. This contamination appeared in a particular region of our detection image, illustrated in Fig. 6. As such we were able to correct for it by subtracting their contribution from the counts collected during measurement shots. Generally, fewer atoms can be attributed to this noise than would be required to explain the discrepancy described in the main text, as illustrated in Fig. 7. While the cause of the cross-contamination is unclear, we observe that the count density outside the region of interest is similar in both the shots with the RF pulse and those without. We hypothesize that the remnant counts are atoms transferred into the $m_J = 0$ state by non-ideal behaviour of the Stern-Gerlach pulses.

As mentioned in the main text, the presence of these counts also prevents a straightforward application of a maximum-likelihood estimator (MLE) to determine parameters of the power-law region. The basic principle of the MLE is to assume a functional form for the probability distribution $p(x|\theta)$ underlying the observed data x , and dependent on some parameters θ ; the zero of the derivative of the *likelihood* function $L(\theta|x)$ with respect to the parameters θ then yields the most-probable parameter values given a set of observations x . In our con-

text, one can assume a functional form for the probability distribution underlying atomic detection events (via a wavefunction ansatz). The detector dark count rates can also be incorporated by assuming a uniform distribution. Such an analytical treatment does not readily permit the inclusion of an empirical density estimate which itself includes the aforementioned dark count rate. Instead, we opt for the simpler approach described in the main text.

C. Peak density calibration

The quantum depletion and contact are both predicted to depend solely on the condensed number and trapping frequencies via the condensate density, hence it is important to determine both quantities accurately. In the Thomas-Fermi approximation, the peak density of the condensate can be written as $n_0 = \mu/g$, where μ is the chemical potential, $g = 4\pi\hbar^2 a_{1,1}/m$ is the effective interaction strength, $m \approx 6.6 \times 10^{-27}$ kg is the atomic mass, and $a = 7.512$ nm is the s-wave scattering length between pairs of atoms in the $m_J = 1$ state [55]. The expression for the peak density can be expanded as

$$n_0 = \frac{1}{8\pi} \left((15N_0)^2 \left(\frac{m\bar{\omega}}{\sqrt{a_{1,1}\hbar}} \right)^6 \right)^{1/5} \quad (5)$$

where $\bar{\omega} = (\omega_x \cdot \omega_y \cdot \omega_z)^{1/3}$ is the geometric trap frequency and N_0 is the number of atoms in the condensate. During these calibration runs we simultaneously determine the total atom number N and trap frequency $\bar{\omega}$ in a single shot using a pulsed atom laser and use the thermal fraction to determine the condensed number N_0 .

The pulsed atom laser consists of a series of Fourier-broadened RF pulses centred on the minimum Zeeman splitting in the trap. The pulse transfers atoms in the trap to the untrapped $m_J = 0$ state with an approximately constant transfer rate across the cloud. We out-couple approximately 2% of the atoms per $100\mu\text{s}$ pulse for ≈ 200 pulses, which eventually depletes the entire trap. The atom laser thus prevents the detector from saturating and allows an accurate determination of the atom number, up to a factor of the quantum efficiency. We determine the trapping frequencies by inducing centre-of-mass oscillations with a magnetic impulse, and finding the oscillation period from the atom laser pulses [56].

III. THEORY

The Hamiltonian of a homogeneous system of interacting bosons, with plane-wave field operators $\hat{a}_{\mathbf{k}}$ labeled by the wavevector $\mathbf{k} = \mathbf{p}/\hbar$, can be diagonalized by the Bogoliubov transformation to a free Bose gas of collective excitations with operators $\hat{b}_{\mathbf{k}}$ [1]. This permits the single-particle momentum density to be written as $\rho(k) = \langle \hat{a}_{\mathbf{k}}^\dagger \hat{a}_{\mathbf{k}} \rangle = (u_{\mathbf{k}}^2 + v_{\mathbf{k}}^2) \langle \hat{b}_{\mathbf{k}}^\dagger b_{\mathbf{k}} \rangle + v_{\mathbf{k}}^2$, where $\hat{a}_{\mathbf{k}} = u_{\mathbf{k}} \hat{b}_{\mathbf{k}} + v_{-\mathbf{k}} \hat{b}_{-\mathbf{k}}^\dagger$, $\hat{a}_{\mathbf{k}}^\dagger = v_{\mathbf{k}} \hat{b}_{\mathbf{k}} + u_{-\mathbf{k}} \hat{b}_{-\mathbf{k}}^\dagger$ and the $u_{\mathbf{k}}$ and $v_{\mathbf{k}}$ terms are fixed by the condensate density, atomic mass, and s-wave scattering length [57, 79]. In the ground state, devoid of thermal excitations, the quasiparticle modes are populated by the $v_{\mathbf{k}}^2$ term [32, 80].

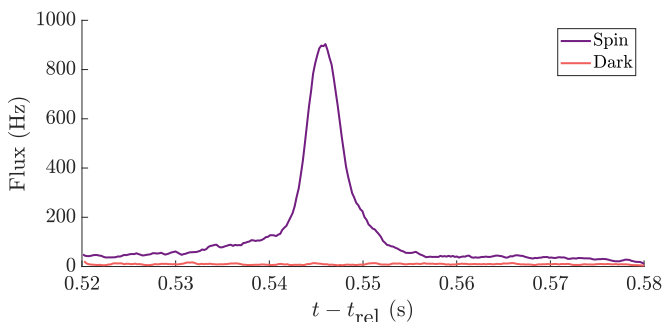


FIG. 6. Measured contribution of the detector dark counts and spurious spin counts to the time-of-flight profile. We accounted for the pulse at around 550ms and subtracted it from the measured profiles when computing the contact. After removing this background term, the density profiles above and below the condensate agree, indicating convergence on the true signal. For reference, the peak flux of the $m_J = 0$ condensate is about a thousandfold greater than the peak shown here.

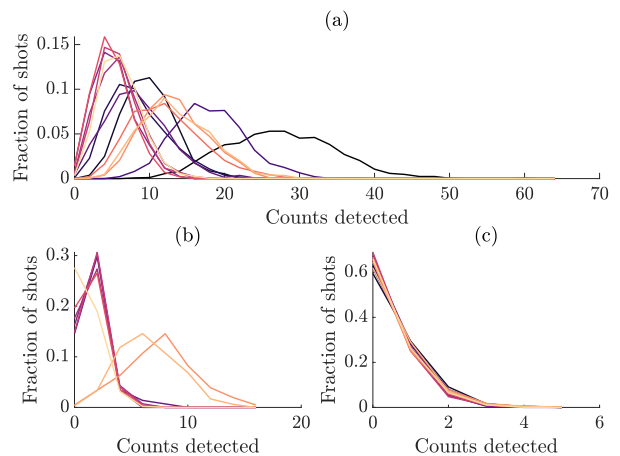


FIG. 7. Number of counts detected in the region of interest in the depletion measurement (a), the spin mixing calibration (b), and the dark count calibration (c). An average of 3.0(5) counts were detected in the ROI in the spin-mixing calibration shot, and the background count rate was 0.4(2) counts per shot. Separate lines indicate separate runs, i.e. sequences of shots with fixed parameters.

While the local-density approximation (LDA) can be employed to compute the amplitude of the k^{-4} tail using the Bogoliubov dispersion [32], the approach opened by Tan's original theorems is simpler than integrating $v_{\mathbf{k}}^2$ across a Thomas-Fermi distribution. The two-body contact is defined by [6]

$$\mathcal{C} = \lim_{k \rightarrow \infty} k^4 \rho(k), \quad (6)$$

where the contact \mathcal{C} is the volume average of the local contact intensity $\hat{C} = 32\pi^2 a^2 \hat{n}^2$ [11]. The contact is related to the total energy E through the *adiabatic sweep theorem* [5],

$$\mathcal{C} = \frac{8\pi m a^2}{\hbar^2} \frac{\partial E}{\partial a}, \quad (7)$$

where a is the s-wave scattering length. In the Thomas-Fermi approximation, the energy per particle of N_0 condensed bosonic atoms is

$$\frac{E}{N_0} = \frac{5}{7} \mu = \frac{5}{7} \frac{\hbar \bar{\omega}}{2} \left(\frac{15 N_0 a}{a_{\text{HO}}} \right)^{2/5}, \quad (8)$$

where $a_{\text{HO}} = \sqrt{\hbar/(m\bar{\omega})}$ is the harmonic oscillator length and $\bar{\omega} = \sqrt[3]{\omega_x \omega_y \omega_z}$ is the geometric trapping frequency [57, 79]. The sweep theorem yields

$$\mathcal{C} = \frac{8\pi}{7} \left(15^2 (a N_0)^7 \left(\frac{m \bar{\omega}}{\hbar} \right)^6 \right)^{1/5}, \quad (9)$$

which shares many factors with the peak density of a harmonically trapped condensate (Eqn. 5), whereby one has

$$\frac{\mathcal{C}}{n_0} = \frac{64\pi^2 a^2}{7} N_0. \quad (10)$$

Peak density (μm^{-3})	$N_{\text{tot}} (\times 10^5)$	Thermal fraction	N_{Detect}	N_{pred}	$C_{\text{est}} (\text{pm}^{-1})$	$C_{\text{est}}/\mathcal{C}$
16(1)	3.5(4)	0.09	5.6(0)	0.7(1)	.2(1)	7(3)
18(1)	5.0(4)	0.17	6.8(1)	0.9(2)	.2(1)	7(2)
19(2)	4.9(6)	0.08	8.1(1)	1.0(2)	.3(1)	7(3)
20(1)	5.7(3)	0.09	14.(1)	1.3(3)	.5(1)	10(3)
38(2)	3.9(3)	0.14	4.9(0)	0.4(1)	.6(3)	10(5)
38(3)	3.7(4)	0.09	3.5(0)	0.4(1)	.4(2)	7(4)
38(3)	3.8(4)	0.11	3.7(1)	0.6(1)	.4(2)	6(3)
38(3)	3.7(4)	0.09	4.1(0)	0.5(1)	.5(2)	7(4)
39(4)	3.8(5)	0.10	4.3(0)	0.5(1)	.5(3)	7(4)
41(2)	4.5(4)	0.12	6.5(1)	0.6(1)	.8(4)	9(5)

TABLE I. Summary of results for each data run. The peak density is determined from measurements of the condensed number (via the total number N_{tot} and condensate fraction) and trapping frequencies, which in turn is used to predict the contact \mathcal{C} . The number N_{Detect} of atoms detected in the region of interest can be used to determine the empirical contact C_{est} from the k^{-4} -like tail, as in the main text, and can be compared to the predicted number of counts N_{pred} . The final column shows the ratio of the estimated to predicted contact, also equal to the ratio of the detected and predicted counts.

By substitution into Eqn. (6) one arrives at the expression

$$\rho(k) = \frac{64\pi^2 a^2 N_0 n_0}{7 k^4} \quad (11)$$

Higher-order effects are negligible in our experiments. The Lee-Huang-Yang (LHY) corrected condensate energy E' for a uniform condensate with density n yields an estimate of the worst-case contribution

$$\frac{\partial E'}{\partial a} = \mathcal{C} \left(1 + \frac{64\sqrt{na^3}}{3\sqrt{\pi}} \right),$$

Where \mathcal{C} is the contact computed neglecting the LHY term, and the second term in brackets is the LHY correction which amounts to at most a correction of order 1%, using the highest n_0 observed in our experiments. In reality the correction will be smaller as the density is not uniform and is bounded above by n_0 .

A. Radio spectroscopic prospects

The cause of the contact anomaly could be elucidated by determining whether it originates in the trapped condensate, or is generated during the trap release and expansion. Such an investigation requires an *in situ* probe of the contact, such as the radio and Bragg spectroscopic techniques. The latter may be the most fruitful of the two simply because of the difficulty of interpreting the results from the former, which we sketch below. The basic principle of RF contact spectroscopy is to apply a monochromatic RF probe which is detuned from the resonance between two spin states, coupling atoms in the initial spin state to an untrapped channel, and then perform a differential measurement of the atom number. The signal strength scales with the difference of reciprocal scattering lengths $\Gamma \propto (1/a_{i,i} - 1/a_{i,f})$ between pairs of atoms in initial-initial ($a_{i,i}$) and initial-final ($a_{i,f}$) spin

states [17, 18], which can be manipulated via Feshbach resonance to obtain a good signal. For He^* (spin 1) however, the scattering lengths $a_{1,1}$ and $a_{1,0}$ are identical [58], rendering the preferred $m_J = 1 - m_J = 0$ transition unusable. On the other hand, $a_{1,-1} = 3/7a_{1,1}$ [59], and the singlet transition can be driven without populating the $m_J = 0$ state. In principle this could produce a detectable flux of atoms to perform sensitive in-trap contact measurements, however, collisions in the $^1\Sigma_g^+$ channel have large Penning ionization rates which lead to significant trap losses [58]. The ionization products would be detectable by in-vacuum channel electron multipliers but require theoretical work to disentangle from the spectroscopic signal. Further, such an experiment could not take advantage of a Feshbach resonance to increase signal strength or decrease the ionization rate. While such a measurement is not *prima facie* impossible, Bragg spectroscopy may yield more comprehensible results.

IV. NUMERICAL SIMULATIONS

A. Evolution

The simulation of the evolution of the cloud is made using an adaptation of the STAB method (stochastic Time-Adaptive Bogoliubov) [34, 35] which uses the positive-P representation [60, 61] to describe Bogoliubov quasiparticles around a dynamically evolving condensate [62]. This allows for straightforward treatment of inhomogeneous and dynamically evolving condensates with their associated quantum depletion, without the need to diagonalise the Bogoliubov de Gennes equations. The systems considered here require $4 - 6 \times 10^6$ modes for simulation, so avoiding diagonalisation is very relevant.

Previous use of the STAB method [34, 35, 53, 63–67] has been according to the equations described in detail in [34] which relied on a separation of the condensate and Bogoliubov quasiparticles in k -space that arose from initial conditions and system dynamics. Here this does not

occur, and there is a significant overlap in momentum space. The standard STAB formulation leads to a bogus amplification of the part of the Bogoliubov field that overlaps with the condensate. Therefore a theory that explicitly imposes orthogonality between condensate and Bogoliubov modes is required. We summarise it below, while details of the derivation and proper benchmarking of the method will be reported in [68].

In terms of operators, the Bose field of the atoms $\widehat{\Psi}(\mathbf{x}, t)$ is written as

$$\widehat{\Psi}(\mathbf{x}, t) = \phi(\mathbf{x}, t) + \widehat{\Psi}_B(\mathbf{x}, t), \quad (12)$$

where $\phi(\mathbf{x}, t)$ is the condensate order parameter described in 3-dimensional space \mathbf{x} , and $\widehat{\Psi}_B(\mathbf{x}, t)$ is a relatively small operator fluctuation field. The smallness requirement can be written

$$N = \int d^3\mathbf{x} |\phi(\mathbf{x}, t)|^2 \quad (13)$$

$$\gg \int d^3\mathbf{x} \langle \widehat{\Psi}_B^\dagger(\mathbf{x}, t) \widehat{\Psi}_B(\mathbf{x}, t) \rangle = N_B = N\delta_B, \quad (14)$$

i.e. N_B the number of particles in the Bogoliubov field is small overall, but locally the Bogoliubov field density

need not be smaller than the condensate – as verified e.g. in [62]. The condition (13) allows one to discard third and higher orders of $\widehat{\Psi}_B$ in the effective Hamiltonian (the Bogoliubov approximation). A second condition, not applied in standard STAB, is

$$\int d^3\mathbf{x} \widehat{\Psi}_B^\dagger(\mathbf{x}, t) \phi(\mathbf{x}, t) = 0. \quad (15)$$

which imposes orthogonality and prevents seeping of condensate atoms into the fluctuation field $\widehat{\Psi}_B(\mathbf{x}, t)$.

The condensate order parameter $\phi(\mathbf{x}, t)$ is assumed to evolve according to the Gross-Pitaevskii equation (correct to leading order, given (13)):

$$i\hbar \frac{d\phi}{dt} = \left[-\frac{\hbar^2}{2m} \nabla^2 + g|\phi|^2 + V(\mathbf{x}, t) \right] \phi. \quad (16)$$

and is normalised to the (conserved) total number of particles $\int d^3\mathbf{x} |\phi(\mathbf{x}, t)|^3 = N$. The $g = 4\pi\hbar^2 a_{1,1}/m$ is the s-wave contact interaction between He* atoms in the initial $m_J = 1$ state (we take $a_{1,1} = 7.51\text{nm}$), and $V(\mathbf{x}, t)$ is the trap potential with in general time-dependent frequency. We then represent the Bogoliubov quasiparticles using the positive-P representation [34, 60], which gives the following equations of motion for the ket $\psi_B(\mathbf{x}, t)$ and bra $\tilde{\psi}_B(\mathbf{x}, t)$ amplitudes of the quasiparticles:

$$i\hbar \frac{d\psi_B}{dt} = \left[-\frac{\hbar^2}{2m} \nabla^2 + g|\phi|^2 + V(\mathbf{x}, t) \right] \psi_B + \mathcal{P}_\perp \left\{ g|\phi|^2 \psi_B + g\phi^2 \tilde{\psi}_B^* + \sqrt{-ig} \phi \xi(\mathbf{x}, t) \right\} \quad (17a)$$

$$i\hbar \frac{d\tilde{\psi}_B}{dt} = \left[-\frac{\hbar^2}{2m} \nabla^2 + g|\phi|^2 + V(\mathbf{x}, t) \right] \tilde{\psi}_B + \mathcal{P}_\perp \left\{ g|\phi|^2 \tilde{\psi}_B + g\phi^2 \psi_B^* + \sqrt{-ig} \phi \tilde{\xi}(\mathbf{x}, t) \right\}. \quad (17b)$$

Here the ket $\psi_B(\mathbf{x}, t)$ and bra $\tilde{\psi}_B(\mathbf{x}, t)$ amplitudes provide the positive-P representation of the Bogoliubov field in 3d space. We used the robust stochastic integration procedure described in [69]. The $\xi(\mathbf{x}, t)$ and $\tilde{\xi}(\mathbf{x}, t)$ are independent white Gaussian noise fields of zero mean and variance

$$\langle \xi(\mathbf{x}, t) \xi(\mathbf{x}', t') \rangle = \langle \tilde{\xi}(\mathbf{x}, t) \tilde{\xi}(\mathbf{x}', t') \rangle \quad (18)$$

$$= \delta^3(\mathbf{x} - \mathbf{x}') \delta(t - t'). \quad (19)$$

An ensemble of field trajectories with independent noise in each trajectory and in each trajectory's initial state is generated to represent the Bogoliubov field. We typically used $\mathcal{S} = 4000$ trajectories.

Notably, the equations (17) allow not only for production of additional Bogoliubov quasiparticles quantum depleted from the condensate but also for their reabsorption.

The main additional element in (17) compared to the standard STAB equations [66] is the projection \mathcal{P}_\perp which imposes the orthogonality requirement (15) and avoids the bogus amplification of the Bogoliubov field where it

overlaps with the condensate. The projection \mathcal{P}_\perp of a field $f(\mathbf{x})$ can be carried out efficiently by

$$\mathcal{P}_\perp f(\mathbf{x}) = f(\mathbf{x}) - \frac{1}{N} \left[\int d^3\mathbf{x} \phi(\mathbf{x})^* f(\mathbf{x}) \right] \phi(\mathbf{x}). \quad (20)$$

The kinetic part of the evolution equations (16)-(17) is also carried out efficiently by a split-step approach which evaluates kinetic terms in k-space and the rest in x-space, moving between k-space and x-space using a fast Fourier transform.

The total quantum depletion of the condensate δ_B is given by

$$\delta_B = \frac{N_B}{N} = \frac{1}{N} \int d^3\mathbf{x} \left\langle \text{Re} \left[\psi_B(\mathbf{x}, t) \tilde{\psi}_B^*(\mathbf{x}, t) \right] \right\rangle_{\text{stoch.}} \quad (21)$$

Stochastic averaging over all trajectories in the ensemble is denoted by $\langle \cdot \rangle_{\text{stoch.}}$. The density of the depleted par-

ticles is evaluated by the standard positive-P expression,

$$n_B(\mathbf{k}) = \left\langle \widehat{\Psi}_B^\dagger(\mathbf{k}, t) \widehat{\Psi}_B(\mathbf{k}, t) \right\rangle \quad (22)$$

$$= \text{Re} \left\langle \widetilde{\psi}_B^*(\mathbf{k}, t) \psi_B(\mathbf{k}, t) \right\rangle_{\text{stoch.}}. \quad (23)$$

The density of condensate

$$n_{BEC}(\mathbf{k}) = (1 - \delta_B) |\phi(\mathbf{k}, t)|^2, \quad (24)$$

is augmented by the $1 - \delta_B$ factor when calculating observables to conserve overall particle number. The k -space fields are

$$\begin{bmatrix} \widehat{\Psi}_B(\mathbf{k}) \\ \psi_B(\mathbf{k}) \\ \widetilde{\psi}_B(\mathbf{k}) \end{bmatrix} = \frac{1}{(2\pi)^{3/2}} \int d^3\mathbf{x} e^{-i\mathbf{k}\mathbf{x}} \begin{bmatrix} \widehat{\Psi}_B(\mathbf{x}) \\ \psi_B(\mathbf{x}) \\ \widetilde{\psi}_B(\mathbf{x}) \end{bmatrix} \quad (25)$$

B. Initial condition

Our simulations aim to study the evolution of the quantum depletion particles in $\widehat{\Psi}_B$ after release from the trap. We use a zero temperature initial condition, since the object is to study the behaviour of the high momentum tails beyond the edge of the thermal cloud. The $T = 0$ initial state is more straightforward to obtain, and also allows us to use lower k -values to access the k^{-4} tails, since they are not obscured by the stronger thermal cloud at intermediate momenta. This significantly reduces the size of the computational lattice needed. For the low temperatures in the experiment we do not expect any significant interaction between the behavior of the thermal cloud and the depleted atoms because both are well approximated by the Bogoliubov Hamiltonian which neglects interactions between excited modes. Therefore the neglect of the thermal cloud does not significantly affect the evolution or properties of the higher k depletion.

However, one cannot use the standard Gross-Pitaevskii ground state since that has 100% condensate and no quantum depletion. The task of generating a cloud with the appropriate depletion in such a large nonuniform system turns out to be nontrivial. Conceptually the issue

is simple – diagonalise the Bogoliubov Hamiltonian, and give the well known Bogoliubov $T = 0$ occupation to each quasiparticle mode. However, for a system with 10^6 modes diagonalisation is not a good option.

A procedure for generating the equilibrium state has been developed in the Wigner representation [62, 70–73]. Unfortunately we cannot use this directly, nor a direct Wigner representation of the quasiparticles because the condition required for correctness of the Wigner representation – that there are more particles than modes – is very far from being met [34, 74, 75]. (In fact here we have about $\mathcal{O}(1000)$ particles, and $\mathcal{O}(10^6)$ modes.). It is also unclear how to translate a local density formulation of depletion in a uniform section of gas to a positive-P ensemble without introducing discontinuities. Instead we turned to dynamically generating a state with the required quantum depletion.

We begin with a fully condensed ground state with $\psi_B = \widetilde{\psi}_B = 0$ and $\phi(\mathbf{x}) = \phi_0(\mathbf{x})$, the ground state of the Gross-Pitaevskii equation (16). The latter is obtained by imaginary time propagation of the GPE augmented with an appropriately chosen chemical potential μ according to (8) which sets the central density.

Our first attempt to generate the equilibrated quantum depleted state thus started with $\phi_0(\mathbf{x})$ and then adiabatically ramped the interaction from $g = 0$ to the experimental value while evolving the equations (16)–(17). This did not work for two reasons. Firstly, a very strong collective oscillation was induced, since the width of the Thomas-Fermi ground state depends strongly on g . Secondly, very long time evolutions succumb to excessive noise in the positive-P simulation and produce a state that is too noisy to be useful. Note that in the positive-P representation different ensembles can represent the same state but exhibit very different noisiness and practical usefulness [76, 77].

The second attempt began with the Gross-Pitaevskii ground state and the physical interaction strength g in the GPE (16), while slowly ramping the interaction strength in the Bogoliubov equations (17). This eliminates the main oscillations in the mean-field evolution. The least unwanted nonadiabatic disturbance occurs when g is ramped only within the projected part of the Bogoliubov evolution as per

$$i\hbar \frac{d\phi}{dt} = \mathcal{H}(g, \phi)\phi = (16) \quad (26a)$$

$$i\hbar \frac{d\psi_B}{dt} = \mathcal{H}(g, \phi)\psi_B + \mathcal{P}_\perp \left\{ g_B |\phi|^2 \psi_B + g_B \phi^2 \widetilde{\psi}_B^* + \sqrt{-ig_B} \phi \xi(\mathbf{x}, t) \right\} \quad (26b)$$

$$i\hbar \frac{d\widetilde{\psi}_B}{dt} = \mathcal{H}(g, \phi)\widetilde{\psi}_B + \mathcal{P}_\perp \left\{ g_B |\phi|^2 \widetilde{\psi}_B + g_B \phi^2 \psi_B^* + \sqrt{-ig_B} \phi \widetilde{\xi}(\mathbf{x}, t) \right\}. \quad (26c)$$

with $g_B(t)$. However, over adiabatic timescales, this still introduced far too much noise in the Bogoliubov fields

$\psi_B, \widetilde{\psi}_B$ to be useful.

To work around the problem, we take advantage of the

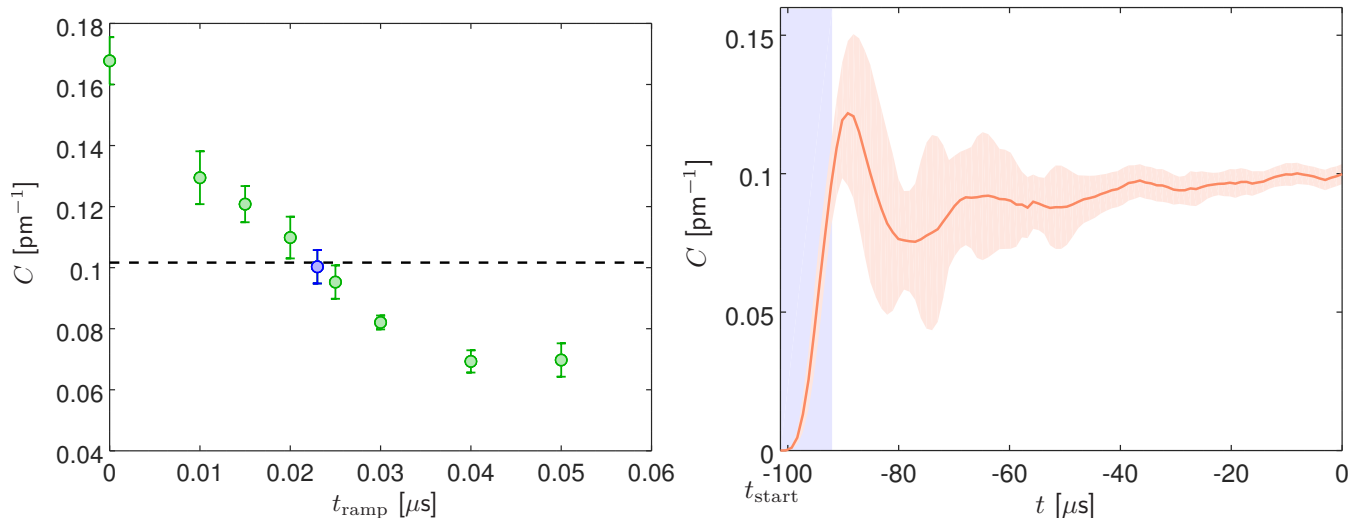


FIG. 8. Details of initial state preparation, shown on the $N = 455852$ case. Left panel: Calibration data. Shown is the calculated contact C at the end of the initial state generation ($t = 0$), as a function of the quench ramp time t_{ramp} . The horizontal dashed line shows the LDA prediction $C = 0.102$ pm⁻¹, the blue data point the simulation that was deemed to agree, and was used for subsequent simulations for $t > 0$. Right panel: Evolution and stabilisation of the contact. The blue shaded area shows the duration of the ramp from t_{start} to $t_{\text{start}} + t_{\text{ramp}}$. Orange shading denotes the error bars. $S = 4000$ trajectories in all cases.

fact that an instantaneous quantum quench of a weakly interacting condensate produces depletion with a similar time-integrated momentum profile $\int dt n_B(\mathbf{k}, t) \propto 1/k^4$ to the ground state value, but with a somewhat higher depletion, as described in detail in [68, 78]. Simulations show that non-instantaneous but rapid quenches produce lower amounts of quantum depletion, as shown in Fig. 8 (left panel). To generate these ensembles, we used the following ramp:

$$g_B(t) = \begin{cases} \left(\frac{t-t_{\text{start}}}{t_{\text{ramp}}}\right) g & \text{when } t < t_{\text{start}} + t_{\text{ramp}} \\ g & \text{when } t \geq t_{\text{start}} + t_{\text{ramp}} \end{cases} \quad (27)$$

starting at negative t_{start} , and evolving till $t = 0$. Thus t_{ramp} was the ramp time, and the remaining time: $|t_{\text{start}}| - t_{\text{ramp}}$ an equilibration time. We carried out a calibration like that shown in Fig. 8 (left panel) for each set of cloud and trap parameters needed. Then for the initial *in situ* ensemble in the trap we chose the ensemble generated with the t_{ramp} that produces total quantum depletion in agreement with the *in situ* value (Eqn 9) for the condensate ground state (like the blue data point in Fig. 8, left panel). The value of t_{start} was $-101\mu\text{s}$ for the weakly trapped cases ($\omega = 425 \times 425 \times 45$ Hz and $\omega = 201$ Hz) and $-198\mu\text{s}$ for the strongly trapped cases ($\omega = 902 \times 895 \times 71$ Hz and $\omega = 393$ Hz) detailed in Table. ???. Fig. 8 (right panel) shows an example of the evolution of the contact *in situ* during this initial state generation.

Properties of the initial states are labelled (CT) and (ST) in Fig. 3 of the main article.

C. Simulation types

Detailed data extracted from the simulations are given in Table. ??. Several types of simulations were made, with shorthand labels as per Fig. 3 of the main article:

(CE) Release of atoms from the trap, as in the experiment. Here the potential was reduced exponentially

$$V(\mathbf{x}) = \frac{m}{2} (\omega_x^2 x^2 + \omega_y^2 y^2 + \omega_z^2 z^2) e^{-t/\tau_{\text{release}}}, \quad (28)$$

with time constant $\tau_{\text{release}} = 37.5\mu\text{s}$. The initial trap frequencies were $\omega = 425 \times 425 \times 45$ Hz and $\omega = 902 \times 895 \times 71$ Hz, and two variants of the initial state were simulated: a low density and a high density cloud.

(CS) A theory work devoted to an analysis of the fate of quantum depletion after release from a trap [33] predicted that no depletion survives – in stark contrast to what we and [32] see experimentally, and to the CE simulations. To test the hypothesis that the difference is due to our system breaking the adiabaticity assumed in [33], we ran simulations in which the trap is not rapidly released, but ramped down in strength over a much longer time period. The timescales here can be compared to the characteristic healing timescale $t_\xi = \hbar/gn_0$ in the centre of the trapped cloud [78]. Here it is $t_\xi = 15 - 40\mu\text{s}$, which is closely comparable to the trap release time τ_{release} , so a suspicion that adiabaticity is strongly broken is warranted. The CS simulations ramped the trap as follows:

$$V(\mathbf{x}) = \frac{m}{2} \left[(\omega_x^2 x^2 + \omega_y^2 y^2) \left(1 - \frac{t}{2t_{\text{ramp}}}\right)^2 + \omega_z^2 z^2 \right], \quad (29)$$

with timescales of order 1-2ms (see Table. ??). The simulations were run up till $t = t_{\text{ramp}}$ when the trap frequency

was half the original one. The *in situ* expressions (Eqn 9) predicts that the depletion should reduce $\propto \bar{\omega}^{6/5}$ to about half its original value. Indeed, such a reduction of depletion was observed, strongly supporting the hypothesis that adiabaticity is needed for agreement with the results of [33]. More detailed study of this will be reported in [68].

(SE) The healing time t_ξ is the typical timescale on which depleted atoms can be produced or *reabsorbed* into the condensate. To avoid the latter and survive trap release, a depleted atom should travel further than the extent of the cloud on this timescale. The velocity distribution of the depletion atoms is isotropic *in situ*, being given by $mv^2/2 \approx gn_0$. Therefore, $v \approx \sqrt{2gn_0/m} = \bar{v}$, which in an isotropic system gives a chance of escape for only the highest k part of the Bogoliubov spectrum with velocities $\gtrsim \bar{v}$. However, the distance to travel to escape reabsorption depends on the cloud shape. In particular, escape is made easier in the tight trap directions (less distance to travel), and harder in the long trap direction. As a check that we have correctly identified the processes involved in depletion survival, we compared release of atoms from the experimental elongated clouds with spherically trapped clouds having the same central density n_0 and particle number N . These clouds had isotropic trapping frequency $\bar{\omega} = (\omega_x \omega_y \omega_z)^{1/3}$ and are labelled (SE). Trap release followed (28) as before. Indeed, as expected we find that the survival of depleted atoms is enhanced in the anisotropic trap compared to the spherical one. Details will be reported in [68].

D. Determination of the contact

Much as in the experiment, the k -space density $n(\mathbf{k})$ in the simulations is very noisy in the asymptotic region of large $|\mathbf{k}|$, and a lot of averaging is needed to extract the contact. We proceed as follows: The simulations provide a density of depleted particles $n_B(\mathbf{k})$. Like with the experimental counts, we keep only density that is far enough away ($\pi/3$ rad) from the long (z) axis of the cloud. We do not restrict counting to the vicinity of the x axis because here there are no detector irregularities to avoid, and this allows us to improve the signal to noise ratio. The simulated system is axially symmetric around the z axis. The particle counts $N_B(\mathbf{k}) = n_B(\mathbf{k})\Delta V_K$ are finely binned according to the absolute value of the momentum $k = |\mathbf{k}|$, giving total bin count N_k . The field is simulated on a square lattice in k space, in which each site corresponds to a k -space volume of ΔV_K . Therefore the total bin volume V_k is obtained by binning the site volumes, and the mean density in each bin is $n_k = N_k/V_k$. Each bin gives an estimate of the corresponding apparent contact:

$$c(k) = n_k k^4 (2\pi)^3 = \frac{N_k}{V_k} k^4 (2\pi)^3. \quad (30)$$

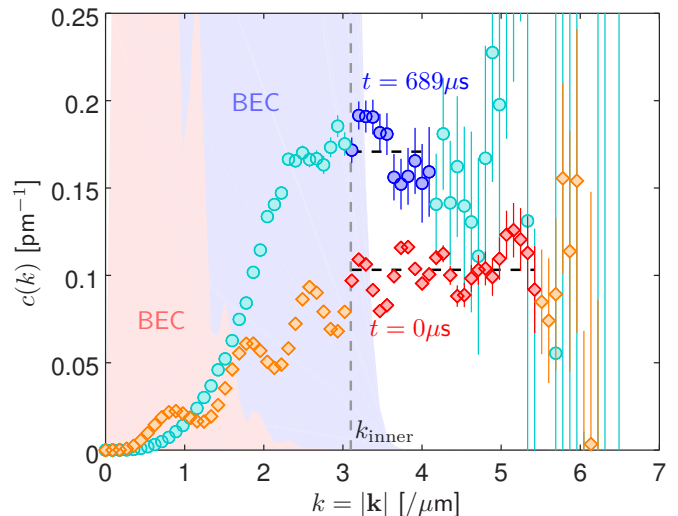


FIG. 9. A busy plot that demonstrates extraction of contact from simulation data – on the example of the $N = 455852$ trap release (CE) simulation. Blue/cyan data: after expansion at $t = 689\mu\text{s}$, Red/orange: *in situ* at $t = 0$. Each data point corresponds to estimation of $c(k)$ given by (30) using the density of particles in the Bogoliubov field $\hat{\Psi}_B(\mathbf{k})$ in a radial bin centred at $k = |\mathbf{k}|$. Error bars give the statistical error from an ensemble of $S = 4000$ trajectories. Blue and red points are the fitted part of the data. The vertical dashed line indicates k_{inner} , while the shaded region on the left shows the corresponding scaled density $c_{\text{BEC}}(k) = n_{\text{BEC}}(k)k^4(2\pi)^3$ that would be calculated from the condensate field $\phi(\mathbf{k})$. The horizontal dashed lines indicate the final estimates of C extracted from the data.

The statistical error estimate on $c(k)$, $\Delta c(k)$, is obtained by averaging subensembles, then using the central limit theorem (CLT) on the subensemble averages. Fig. 9 shows example values and error estimates.

We can see that for a significant range of k values the $c(k)$ estimate gives fluctuations around a constant value. However, several difficulties in extracting the overall trend are also evident. Low k values are not representative because the particles in the shaded region never emerge from the condensate and are not measured in the experiment. Therefore we remove data below a value k_{inner} from consideration. k_{inner} is chosen such that it does not include any depletion that would significantly overlap with the BEC in the final expanded cloud and be obscured by it. This corresponds also to the energy at which the quasiparticle spectrum becomes particle-like, since the mean field energy in the centre of the trapped cloud is responsible for both effects.

High k values, on the other hand, suffer from statistical error sufficiently high as to make them useless, and so we also choose a maximum k_{outer} value, and only use $k \in [k_{\text{inner}}, k_{\text{outer}}]$ to extract the contact estimate. The useless high k region changes with time during the simulation. To systematically adapt our fitting region to this, we choose k_{outer} according to the calculated statistical

error such that

$$\Delta c(k, t) \leq \Delta_{\max} \quad \forall k \leq k_{\text{outer}}(t), \quad (31)$$

and Δ_{\max} is chosen once for all times in a simulation. This gives a time-dependent fitting region $k \in [k_{\text{inner}}, k_{\text{outer}}(t)]$. The final contact estimate $C(t)$ is the mean of all $c(k, t)$ values in the fitting range. Error bars on $C(t)$, $\Delta C(t)$, are obtained from a CLT estimate of the error in the mean of the points used, after binning enough neighbouring points to encompass the autocorrelation (i.e. so that neighbouring bins are uncorrelated). The Δ_{\max} is chosen low enough so that the statistical error in individual points $\Delta c(k, t)$ at the large k end does not put off the overall contact estimation $C(t) \pm \Delta C(t)$. Operationally we choose the value of Δ_{\max} at which the error introduced by adding successive high k points introduces more uncertainty than the reduction thanks to a larger ensemble.

Trap at $t = 0$ ω (Hz)	Peak density n_0 at $t = 0$ (μm^{-3})	N	$n_o N$ ($10^6 \mu\text{m}^{-3}$)	timescale (μs)	Time t (μs)	$C(t)$ (pm^{-1})	$C(t)/C(0)$	$N_B(t)$	$k_{\text{inner}}-k_{\text{outer}}$ (μm^{-1})	Δ_{max} (μm^{-1})
In situ initial state (CT,ST):										
$425 \times 425 \times 45$	16.82(5)	311360	5.237(16)	$t_B=19.8$	0	0.0260(13)	–	1391(7)	2.1–4.2	0.025
$425 \times 425 \times 45$	21.32(10)	567180	12.09(6)	$t_B=15.8$	0	0.060(5)	–	2860(13)	2.2–4.75	0.032
$902 \times 895 \times 71$	32.17(13)	213293	6.86(3)	$t_B=8.5$	0	0.034(4)	–	1324(6)	2.9–4.9	0.020
$902 \times 895 \times 71$	43.66(18)	455852	19.90(8)	$t_B=9.3$	0	0.100(3)	–	3047(12)	3.25–5.4	0.032
$201 \times 201 \times 201$	16.88(6)	316766	5.35(2)	$t_B=19.8$	0	0.025(3)	–	1396(7)	2.1–4.1	0.025
$201 \times 201 \times 201$	21.32(10)	573650	12.23(6)	$t_B=14.2$	0	0.060(9)	–	2741(11)	2.2–4.15	0.04
$393 \times 393 \times 393$	44.15(21)	461514	20.38(10)	$t_B=7.7$	0	0.101(5)	–	3107(12)	3.0–5.0	0.025
Rapid release from trap (CE,SE), $\tau_{\text{release}} = 37.5\mu\text{s}$:										
$425 \times 425 \times 45$	16.82(5)	311360	5.237(16)	τ_{release}	1583	0.0386(22)	1.49(11)	910(20)	2.1–2.8	0.020
$425 \times 425 \times 45$	21.32(10)	567180	12.09(6)	τ_{release}	1346	0.090(7)	1.51(17)	1880(40)	2.3–3.05	0.020
$902 \times 895 \times 71$	32.17(13)	213293	6.86(3)	τ_{release}	689	0.057(5)	1.69(14)	950(20)	2.8–3.7	0.03
$902 \times 895 \times 71$	43.66(18)	455852	19.90(8)	τ_{release}	689	0.171(10)	1.66(12)	2300(40)	3.1–4.1	0.06
$201 \times 201 \times 201$	16.82(5)	316766	5.35(2)	τ_{release}	1900	0.025(3)	1.02(15)	780(30)	1.9–2.65	0.025
$201 \times 201 \times 201$	21.32(10)	573650	12.23(6)	τ_{release}	1900	0.066(7)	1.11(20)	1630(50)	2.3–3.15	0.05
$393 \times 393 \times 393$	44.15(21)	461514	20.38(10)	τ_{release}	973	0.110(5)	1.09(8)	1780(50)	3.1–3.8	0.05
Slow ramp down of trap (CS):										
$425 \times 425 \times 45$	16.82(5)	311360	5.237(16)	$t_{\text{ramp}}=2375$	2375	0.010(3)	0.40(12)	1750(140)	1.9–3.45	0.030
$425 \times 425 \times 45$	21.32(10)	567180	12.09(6)	$t_{\text{ramp}}=2375$	2375	0.020(3)	0.35(7)	2700(300)	2.0–3.9	0.040
$902 \times 895 \times 71$	32.17(13)	213293	6.86(3)	$t_{\text{ramp}}=1216$	1216	0.011(6)	0.3(2)	1520(150)	2.5–4.2	0.040
$902 \times 895 \times 71$	43.66(18)	455852	19.90(8)	$t_{\text{ramp}}=1216$	1216	0.044(5)	0.45(6)	3800(400)	2.5–4.1	0.035
Instantaneous switch-off of the trap:										
$902 \times 895 \times 71$	43.66(18)	455852	19.90(8)	$t_{\text{ramp}}=0$	689	0.0187(6)	1.80(6)	2380(40)	3.1–4.05	0.05

TABLE II. Main simulation data and parameters. The time t for which data are calculated is counted relative to the start of the trap release. Abbreviations (CT,CE,...) as in Figure 3a of the main text. The range $k_{\text{inner}}-k_{\text{outer}}$ was chosen as explained in the text and used to obtain the estimate and uncertainty for C . In all cases, $\mathcal{S} = 4000$ trajectories averaged. N_B is the number of Bogoliubov field particles as per (21).